

# Initial-Offset-Control Coexisting Hyperchaos in Two-Dimensional Discrete Neuron Model

Han Bao , Member, IEEE, Zhuowu Wang , Zhongyun Hua , Senior Member, IEEE, Xihong Yu , Quan Xu , Member, IEEE, and Bocheng Bao , Member, IEEE

**Abstract**—Designing low-dimensional discrete maps with initial-dependent coexisting property is an attractive but challenging task. The coexisting property of a discrete map can be featured by initial-offset-control dynamics. To this end, this article proposes a two-dimensional discrete neuron model with sine activation function. The mechanisms of initial-offset-control coexisting dynamics are theoretically investigated and the homogenous coexisting behaviors are numerically revealed. The results show that the homogenous coexisting attractors are controlled along one direction by one initial-offset and along two directions by two initial-offsets. The former makes it model own finite invariant points, while the latter makes it own infinite invariant points. The homogenous coexisting hyperchaotic attractors are experimentally acquired on field programmable gate array digital platform. Besides, eight pseudorandom number generators (PRNGs) are designed using the proposed model under different parameter and initial settings, and the test results by TestU01 test suite show the high randomness of these PRNGs without chaos degradation.

**Index Terms**—Chaos degradation, coexisting dynamics, discrete neuron model, initial-offset, pseudorandom number generator, TestU01 test suite.

## I. INTRODUCTION

AS THE basic building blocks of the brain, neurons and their networks can show complex chaotic dynamics [1]. There has been evidence that neurons generate firing activities in a regime called chaos edges, which may be central to complexity, learning efficiency, adaptability, and analog computation in brains [2]. The study of the chaotic dynamics in neuron models and neural networks is of great significance, because they have important potential applications in many fields, such as

Manuscript received 23 April 2023; revised 22 July 2023; accepted 2 October 2023. Date of publication 14 November 2023; date of current version 23 February 2024. This work was supported in part by the National Natural Science Foundation of China under Grant 62201094, Grant 62271088, and Grant 12172066. Paper no. TII-23-1399. (Corresponding author: Bocheng Bao.)

Han Bao, Zhuowu Wang, Xihong Yu, Quan Xu, and Bocheng Bao are with the School of Microelectronics and Control Engineering, Changzhou University, Changzhou 213159, China (e-mail: hanbao@cczu.edu.cn; wang\_zw19851921213@163.com; xihongyuyu@163.com; xuquan@cczu.edu.cn; mervinbao@126.com).

Zhongyun Hua is with the School of Computer Science and Technology, Harbin Institute of Technology, Shenzhen, Guangdong 518055, China (e-mail: huazhum@gmail.com).

Color versions of one or more figures in this article are available at <https://doi.org/10.1109/TII.2023.3327566>.

Digital Object Identifier 10.1109/TII.2023.3327566

neuromorphic learning [3], unsupervised learning [4], and digit image recognition [5]. With more knowledge about the dynamics of neural networks, not only reasonable explanations of their complex dynamics can be made, but also appropriate control strategies can be developed to achieve the desired dynamics of artificial neural networks [6]. As a result, chaotic dynamics of neuron models and their neural networks have received growing and extensive attention [7], [8].

The neuron models and their neural networks with different nonlinearities belong to autonomous or nonautonomous nonlinear dynamical systems with continuous-time or discrete-time expressions [9], [10]. By contrast, a discrete neuron model, like most discrete dynamical systems, can generate complex dynamics such as chaos and hyperchaos with low-dimensional and simple algebraic structure. Therefore, the discrete neuron model can also generate chaotic sequences with excellent performance and is applied in the industrial field [11]. However, many chaotic systems exhibit weak chaos, which manifests that their chaotic behaviors are frail and even small perturbations to their control parameters may cause chaos degradation [12]. Such chaotic systems have proved to be unsuitable for practical applications [13]. In fact, some chaotic systems with simple dynamical behaviors may lead to serious security problems, due to their limited performance such as easy occurrence of chaos degradations [14]. Therefore, designing chaotic systems with high ability to resist chaos degradation greatly contributes to the chaos theory and chaos-based applications.

Theoretically, hyperchaos with at least two positive Lyapunov exponents is a more complex nonlinear phenomenon than chaos, and the hyperchaotic sequences usually have high security in many industrial applications such as secure communication [15], [16]. To produce hyperchaos, continuous dynamical systems need at least four dimensions, while discrete dynamical systems need only two. Sine chaotification map [17], nonautonomous memristive map [18], and sine-transform-based memristive model [19] are two-dimensional (2-D) discrete systems, but they can produce hyperchaos. The chaotification schemes and memristor nonlinearities can easily increase the chaos complexity of existing discrete systems. Recently, by employing modular chaotification, a general 2-D parametric polynomial system was proposed in [20], which can generate multiple 2-D hyperchaotic maps, thus obtaining robust hyperchaos with desired complexity. Meanwhile, by coupling memristor nonlinearity, a general three-dimensional (3-D) memristive map model was constructed in [21], which can derive four specific

3-D memristive maps to acquire hyperchaotic sequences with high randomness. Besides, discrete systems with low-dimensional algebraic structures can also demonstrate the same dynamics diversity and chaos complexity as continuous systems [22], but they are easier to be implemented in digital circuits and require much lower compute resources in industrial applications compared to continuous systems [17]. In conclusion, it is a very interesting topic to design discrete hyperchaotic systems with high randomness with high ability to resist chaos degradation.

Initial-offset-control coexisting dynamics is a special kind of multistability, and it is an inherent property of chaotic systems. A simple method to achieve coexisting dynamics is to introduce periodic nonlinearities into some existing offset-boostable systems [23]. The newly constructed chaotic systems readily provide infinitely many invariant points, and thus allow the coexistence of initial-offset-control homogeneous multiple attractors herein. For example, Njitacke et al. [24] considered a 3-D nonautonomous model of memristive tabu learning neuron to provide homogeneous coexisting chaotic attractors. Zhang et al. [25] proposed a memristive autapse-coupled neuron model to discover hidden coexisting homogeneous bursting firings with different offsets. Lin et al. [26] applied a multipiecewise memristive synapse control to a Hopfield neural network to generate the coexisting multiple attractors. However, this method was mainly applied to continuous chaotic systems, and it is difficult to give theoretical analysis.

Recently, by introducing three sinusoidal functions into a map, a self-reproduction hyperchaotic map was constructed and its compound lattice dynamics with uncontrolled attractor growth was disclosed [27]. Inspired by this, this article proposes a novel 2-D discrete neuron model (2D-DNM) with simple periodic activation function, which is derived from the continuous model of tabu learning neuron [28]. Interestingly, by setting the initial-offsets, homogeneous coexisting line/plane hyperchaos can be uncovered and controlled in such 2D-DNM, unlike the coexisting hyperchaos with uncontrolled attractor growth given in [27]. Particularly, the pseudorandom number generators (PRNGs) designed in this article can pass the rigorous test of TestU01 standard, reflecting the strong robustness without chaos degradation. Such a low-dimensional discrete chaotic map with simple algebraic structure was not reported yet. In addition, following the proposed criteria for detecting new chaotic systems in [29], 2D-DNM is based on an existing neuron model, which not only possesses a simple and low-dimensional structure, but also exhibits the coexisting line/plane hyperchaos unobserved previously.

The contributions of this article are outlined as follows.

- 1) We propose 2D-DNM with sine activation function based on the continuous model of tabu learning neuron.
- 2) We theoretically investigate the mechanisms of initial-offset-control coexisting dynamics and numerically reveal the homogeneous coexisting behaviors.
- 3) We experimentally acquire the initial-offset-control homogeneous coexisting hyperchaos on FPGA digital platform.

- 4) We design eight PRNGs using the model under eight control parameter and initial condition settings and analyze their randomness using TestU01 test suite.

The rest of this study is organized as follows. Section II proposes 2D-DNM and investigates the stability of its invariant point. Section III investigates the initial-offset-control mechanism theoretically and reveals the homogenous coexisting dynamics numerically. Section IV studies the digital implementation on FPGA technology. Section V designs eight PRNGs and analyzes their randomness using TestU01 test suite. Finally, Section VI summarizes this article.

## II. TWO-DIMENSIONAL DISCRETE NEURON MODEL

In this section, we derive a 2D-DNM from the continuous model of tabu learning neuron and investigate the stability of its invariant point.

### A. Description of Discrete Neuron Model

According to Li et al. [28], the continuous model of tabu learning neuron is a 2-D dynamical system described by ordinary differential equations, which is expressed mathematically as follows:

$$\begin{aligned}\dot{u}(t) &= -au(t) + bf(u(t)) + J(t), \\ \dot{J}(t) &= -\alpha J(t) - \beta f(u(t)),\end{aligned}\quad (1)$$

where  $u(t)$  and  $J(t)$  stand for the neuron state and the tabu learning state, respectively,  $a$ ,  $b$ ,  $\alpha$ , and  $\beta$  are four control parameters, and  $f(\bullet)$  stands for the activation function. When applying a sinusoidal stimulus, this continuous model given in (1) can exhibit chaotic dynamics.

Using the discrete modeling method, the discrete model of tabu learning neuron is derived from (1), which is described mathematically as follows [30]:

$$\begin{aligned}x_{n+1} &= -x_n + af(x_n) + y_n, \\ y_{n+1} &= -by_n - cf(x_n),\end{aligned}\quad (2)$$

where  $a$ ,  $b$ , and  $c$  are three control parameters,  $n$  is the iteration over time,  $x_n$  and  $y_n$  represent the discrete states of  $u(t)$  and  $J(t)$  at the  $n$ th iteration, respectively. Thus, 2D-DNM is presented in (2), which only involves the nonlinearity of the activation function  $f(x)$ .

The activation function of neuron is a differentiable function with upper and lower bounds. Biologically, during polarization and depolarization, the mediators and cells of neurons can be magnetized and polarized in turn. In particular, periodic firing activity can regulate the propagation, pumping, and distribution of ions in the cell. Therefore, a periodic activation function can be used to estimate polarization characteristics. With this knowledge and for simplicity, the activation function selected here can be expressed as follows:

$$f(x) = \sin(x). \quad (3)$$

The activation function described in (3) is the sinusoidal function, which is periodically multivalued. However, the activation function used in [24] and [30] is the hyperbolic tangent function

and that used in [31] is the piecewise-linear sign function, both of which are monotonously single-valued. And the activation function used in [28] and [32] is the complicated exponential function, which is nonmonotone dual-valued. In contrast, the activation function described in (3) is simple and quite different from those used in the literature.

### B. Invariant Point and Its Stability

The invariant point of 2D-DNM in (2) is assumed as  $P = (X, Y)$ , which can be solved from  $X = -X + a \sin X + Y$  and  $Y = -bY - c \sin X$ . So one obtains the following:

$$P = (X, Y) = \left( X, \frac{2c}{c-a-ab} X \right) \quad (4)$$

where  $X$  can be obtained from the following equation:

$$\sin X + \frac{2(1+b)}{c-a-ab} X = 0. \quad (5)$$

Thus, the solutions of (5) are multiple and changeable, dependent on the control parameters. It should be noticed that when  $b = -1$ , (5) has infinite solutions, which makes 2D-DNM own infinitely many invariant points; otherwise, when  $b$  is free of arbitrary constants other than  $-1$ , (5) has finite solutions, which makes 2D-DNM own finite invariant points.

Correspondingly, the Jacobian matrix at the invariant point  $P$  is yielded from (2) and (3) as follows:

$$\mathbf{J}_P = \begin{bmatrix} -1 + a \cos X & 1 \\ -c \cos X & -b \end{bmatrix}. \quad (6)$$

And the characteristic polynomial is obtained as follows:

$$P(\lambda) = \lambda^2 + d_1\lambda + d_2 \quad (7)$$

where  $d_1 = 1 + b - a \cos X$ ,  $d_2 = b - (ab - c) \cos X$ . So the eigenvalues of the Jacobian matrix are solved from (7) as follows:

$$\lambda_{1,2} = -0.5d_1 \pm 0.5\sqrt{d_1^2 - 4d_2}. \quad (8)$$

From the  $\lambda_{1,2}$  of (8), the stability types of invariant points can be summarized as the following cases. 1) If  $|\lambda_1| < 1$  and  $|\lambda_2| < 1$ ,  $P$  is a stable point (SP). 2) If  $|\lambda_1| > 1$  or  $|\lambda_2| > 1$ ,  $P$  is an unstable point (UP). 3) if  $|\lambda_1| < 1$  and  $\lambda_2 = -1$ , or if  $\lambda_1 = -1$  and  $|\lambda_2| < 1$ ,  $P$  is a period-doubling bifurcation point (PBP). 4) If  $\text{Re}(\lambda_{1,2}) < 1$  and  $|\lambda_{1,2}| = 1$ ,  $P$  is a Neimark–Sacker bifurcation point (NBP). Therefore, the invariant points in cases 3) and 4) are two critical points, leading to the emergence of the period-doubling bifurcation or the Neimark–Sacker bifurcation.

For 2D-DNM, the control parameters  $a$  and  $b$  are set to two groups of typical settings, and the control parameter  $c$  is determined to be a value that varies between  $-4$  and  $4$ . From (4) and (8), the invariant points with different stability types can be calculated for different values of  $c$ . When  $a = 0.6$  and  $b = -0.4$ , the numerical result is shown in Fig. 1(a), while when  $a = -0.6$  and  $b = -1$ , the numerical result is shown in Fig. 1(b). Here SP and UP are marked in black and red, and PBP and NBP are marked with bold green and blue stars, respectively. As shown in Fig. 1(a), when increasing  $c$ , three invariant points appear at

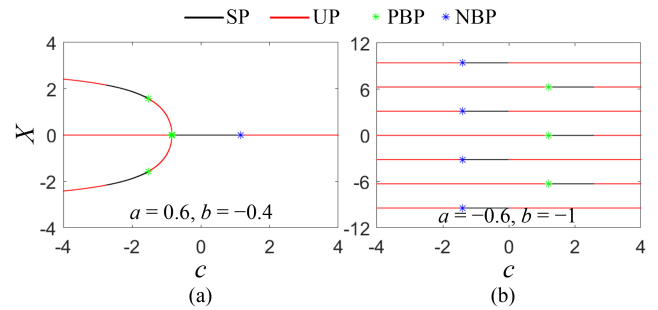


**Fig. 1.** For different control parameters, the invariant points and their stability types for different values of  $c$ . The ordinate value of each point on the line segment is the value of the invariant point  $P$  on the  $X$ -axis, and the colors on the line segment are the stability types. (a) For fixed  $a = 0.6$ ,  $b = -0.4$ . (b) For fixed  $a = -0.6$ ,  $b = -1$ .

the beginning and merge into one invariant point at  $c = -0.84$ . In the interval  $c \in [-2.758, -1.525]$ , the three invariant points contain two SPs and one UP, while in the interval  $c \in [-0.84, 1.16]$ , the unique invariant point is a SP, resulting in the stable state in 2D-DNM. However, as shown in Fig. 1(b), there are an infinite number of invariant points, and in the intervals of  $c \in [-1.4, 0]$  and  $c \in [1.2, 2.6]$ , half of the UPs and half of the SPs are separated from each other by  $\pi$  on the  $X$ -axis. In particular, with the change of  $c$ , the two stability types of the invariant points are transferred by PBPs and NBPs, leading to complex dynamics in 2D-DNM.

### III. INITIAL-OFFSET-CONTROLLED COEXISTING DYNAMICS

Because the nonlinear function  $\sin(x)$  in (3) is periodic, 2D-DNM has homogenous coexisting behaviors regulated by the initial conditions under some specific control parameters. In this section, we investigate the control mechanism theoretically and reveal the homogenous coexisting dynamics numerically.

To facilitate theoretical analysis, 2D-DNM can be rewritten as follows:

$$\begin{aligned} x_{n+1} &= -x_n + a \sin x_n + y_n, \\ y_{n+1} &= -by_n - c \sin x_n \end{aligned} \quad (9)$$

where  $n = 1, 2, 3, \dots$ ,  $x$  and  $y$  are two state variables. Given that 2D-DNM has finite or infinite invariant points under different control parameter  $b$ , the mathematical model in (9) can be divided into two categories, i.e., *Case 1*:  $b = \text{Any Constant}$  and *Case 2*:  $b = -1$ .

#### A. Control Mechanism of Case 1: $b = \text{Any Constant}$

The initial conditions of 2D-DNM are denoted as  $(x_0, y_0)$ . If  $x_0$  is regulated by an offset  $2m\pi$  ( $m$  is a natural number) and  $y_0$  remains unchanged, i.e., the new initial conditions  $(x'_0, y'_0) = (x_0 + 2m\pi, y_0)$ , 2D-DNM generates new iterative sequences that are denoted by state variables  $(x', y')$ . Thus, for  $(x'_0, y'_0)$ , the new iterative sequences after the first iteration are expressed as follows:

$$\begin{cases} x'_1 = x_0 + 2m\pi = x_1 + 2m\pi, \\ y'_1 = y_0 = y_1 \end{cases} \quad (10)$$

the iterative sequences after the second iteration become

$$\begin{aligned} x'_2 &= -x_1 - 2m\pi + a \sin(x_1 + 2m\pi) + y_1 = x_2 - 2m\pi, \\ y'_2 &= -by_1 - c \sin(x_1 + 2m\pi) = y_2 \end{aligned} \quad (11)$$

and the iterative sequences after the third iteration become

$$\begin{aligned} x'_3 &= -x_2 + 2m\pi + a \sin(x_2 - 2m\pi) + y_2 = x_3 + 2m\pi, \\ y'_3 &= -by_2 - c \sin(x_2 - 2m\pi) = y_3. \end{aligned} \quad (12)$$

In succession, the iterative sequences after the  $(n+1)$ th iteration can be described in the general form as follows:

$$\begin{aligned} x'_{n+1} &= x_{n+1} + (-1)^n 2m\pi, \\ y'_{n+1} &= y_{n+1}. \end{aligned} \quad (13)$$

Consequently, the solution of (9), i.e., the iterative sequence of the new state variable  $x'$ , is linearly shifted by  $(-1)^n 2m\pi$  offset along the  $x$ -coordinate when  $x_0$  is regulated by an offset  $2m\pi$ . In other words, the linear transformation between the original iterative sequence and the new iterative sequence can be rewritten as follows:

$$\begin{cases} x' \rightarrow x + 2m\pi \text{ for even } n, \\ x' \rightarrow x - 2m\pi \text{ for odd } n. \end{cases} \quad (14)$$

It means that when  $x_0$  is regulated by an offset  $2m\pi$ , the iterative sequence of  $x'$  has paired mirror shifts with the  $2m\pi$  offset and  $-2m\pi$  offset along the  $x$ -coordinate, respectively.

Similarly, for the new initial conditions  $(x'_0, y'_0) = (x_0 - 2m\pi, y_0)$ , the linear transformation given in (14) is changed as follows:

$$\begin{cases} x' \rightarrow x - 2m\pi \text{ for even } n, \\ x' \rightarrow x + 2m\pi \text{ for odd } n. \end{cases} \quad (15)$$

From the above expression, when  $x_0$  is regulated by an offset  $-2m\pi$ , the iterative sequence of  $x'$  has the same paired mirror shifts along the  $x$ -coordinate. Therefore, only the case where  $x_0$  is positive regulation is discussed for 2D-DNM.

### B. Control Mechanism of Case 2: $b = -1$

More interestingly, when  $b = -1$ , 2D-DNM shows a special case in which the attractor dynamic amplitudes can be flexibly regulated by the initial conditions. To prove this special case, we just have to demonstrate that 2D-DNM can be regulated by the initial condition  $y_0$  along the  $y$ -coordinate.

For  $(x_0, y_0)$  and  $(x, y)$ , a new set of initial conditions is regulated as  $(x'_0, y'_0) = (x_0, y_0 \pm 2l\pi)$  ( $l$  is a natural number), 2D-DNM can generate new iterative sequences corresponding to  $(x', y')$ . Thus, for  $(x_0, y_0 \pm 2l\pi)$ , the new iterative sequences after the first iteration can be described as follows:

$$\begin{cases} x'_1 = x_0 = x_1, \\ y'_1 = y_0 \pm 2l\pi = y_1 \pm 2l\pi. \end{cases} \quad (16)$$

After the second iteration, the iterative sequences become

$$\begin{cases} x'_2 = -x_1 + a \sin x_1 + y_1 \pm 2l\pi = x_2 \pm 2l\pi, \\ y'_2 = (y_1 \pm 2l\pi) - c \sin x_1 = y_2 \pm 2l\pi \end{cases} \quad (17)$$

where  $b = -1$  is used. After the third iteration, the iterative sequences further become

$$\begin{cases} x'_3 = -x_2 \mp 2l\pi + a \sin x_2 + y_2 \pm 2l\pi = x_3, \\ y'_3 = (y_2 \pm 2l\pi) - c \sin x_2 = y_3 \pm 2l\pi. \end{cases} \quad (18)$$

Similarly, after the  $(n+1)$ th iteration, the iterative sequences can be described in the general form as follows:

$$\begin{cases} x'_{n+1} = x_{n+1}, \\ y'_{n+1} = y_{n+1} \pm 2l\pi \end{cases} \quad (19a)$$

for  $n = 1, 3, 5, \dots$ , or

$$\begin{cases} x'_{n+1} = x_{n+1} \pm 2l\pi, \\ y'_{n+1} = y_{n+1} \pm 2l\pi \end{cases} \quad (19b)$$

for  $n = 2, 4, 6, \dots$ .

In summary, when  $y_0$  is regulated by an offset  $\pm 2l\pi$ , the linear transformation between the original iterative sequence and the new iterative sequence can be rewritten as follows:

$$\begin{cases} \begin{cases} x' \rightarrow x \\ y' \rightarrow y \pm 2l\pi \end{cases} \text{ for odd } n, \\ \begin{cases} x' \rightarrow x \pm 2l\pi \\ y' \rightarrow y \pm 2l\pi \end{cases} \text{ for even } n. \end{cases} \quad (20)$$

According to (20), when  $y_0$  is regulated by an offset  $\pm 2l\pi$ , the iteration sequence of the new state variable  $x'$ , one of which remains unchanged and the other is shifted with the offset  $\pm 2l\pi$  along the  $x$ -coordinate, whereas the new state variable  $y'$  is shifted with the offset  $\pm 2l\pi$  along the  $y$ -coordinate.

It should be specially pointed out that when  $b = -1$ , the invariant point of 2D-DNM can be solved as follows:

$$P = (X, Y) = (\pm k\pi, \pm 2k\pi), \quad (21)$$

where  $k$  is a natural number. Thus, 2D-DNM has infinitely many invariant points and presents a grid distribution on the  $X - Y$  plane. In other words, 2D-DNM has infinitely many grid invariant points. For these grid invariant points, the two eigenvalues in (8) can be simplified as follows:

$$\begin{cases} \lambda_{1,2} = 0.5a \pm 0.5\sqrt{(a-2)^2 - 4c} & \text{for even } k, \\ \lambda_{1,2} = -0.5a \pm 0.5\sqrt{(a+2)^2 + 4c} & \text{for odd } k. \end{cases} \quad (22)$$

It indicates that the stability of the grid invariant points depends not only on the control parameters  $a$  and  $c$ , but also on the grid positions of these invariant points.

### C. Homogenous Coexisting Behaviors for Case 1

For Case 1, we set the control parameters and initial conditions as  $a = 0.6$ ,  $b = -0.4$ , and  $(x_0, y_0) = (0.1 + 2m\pi, 0)$  ( $m = 0, 1, 2, 3$ ). When the model parameter  $c$  increases from  $-3.39$  to  $3$ , the homogenous coexisting behaviors regulated by the initial conditions can be simulated numerically. Fig. 2(a) depicts the bifurcation diagrams of state variable  $x$  under four sets of initial conditions, and Fig. 2(b) plots the LE spectra under the initial conditions  $(0.1, 0)$ .

As can be seen from Fig. 2, the bifurcation diagrams under these four sets of initial conditions have the same bifurcation structure but different dynamic amplitudes. With the increment

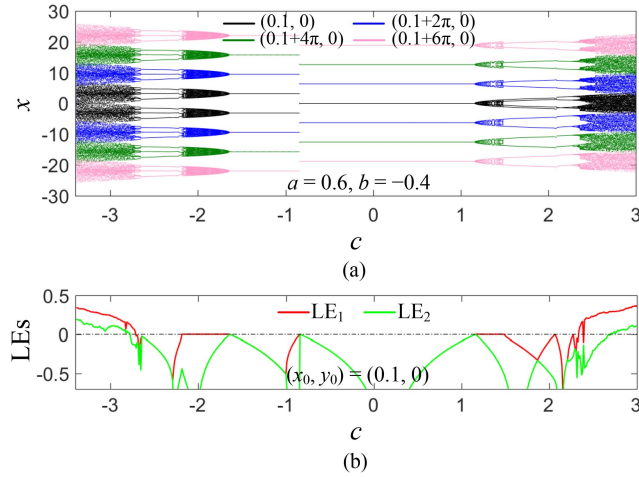


**Fig. 2.** For  $a = 0.6$ ,  $b = -0.4$ , and  $(x_0, y_0) = (0.1 + 2m\pi, 0)$  ( $m = 0, 1, 2, 3$ ) with  $c \in [-3.39, 3]$ , homogenous coexisting behaviors regulated by the initial conditions. (a) Bifurcation diagrams of state variable  $x$  under  $(x_0, y_0) = (0.1 + 2m\pi, 0)$ . (b) LE spectra under  $(x_0, y_0) = (0.1, 0)$ .

of the control parameter  $c$ , 2D-DNM has the quasi-periodic route to chaos and shows complex dynamical behaviors of hyperchaos having two positive LEs, chaos having one positive LE, quasi-period having one zero LE, period having two negative LEs, and stable point having two negative LEs. Specifically, as  $c$  varies in the interval  $[-3.39, -0.84]$ , the bifurcation diagram under the initial conditions  $(0.1, 0)$  has two seed track bands (black) and the corresponding attractors are called twin seed attractors; whereas as  $c$  varies in the interval  $[-0.84, 3]$ , the bifurcation diagram under  $(0.1, 0)$  has one seed track band (black) and the corresponding attractors are called single seed attractors. More specifically, when the initial condition  $x_0$  is regulated by the offset  $2m\pi$ , so that in  $c \in [-3.39, -0.84]$ , the upper and lower seed track bands of the bifurcation diagram are shifted by the offset  $2m\pi$  along the positive and negative  $x$ -coordinates, respectively, while in  $c \in [-0.84, 3]$ , the seed track band of the bifurcation diagram splits into two track bands and they are shifted by the offset  $2m\pi$  along the positive and negative  $x$ -coordinates, respectively.

Additionally, as 2D-DNM is multistable, the bifurcation diagrams shown in Fig. 2 can also be depicted using both forward and backward methods exposed in [29]. To represent the initial-boosted coexisting behaviors more directly, in this article, we select four sets of determined initial conditions according to the theoretical results given above, and show the initial-boosted coexisting bifurcation behaviors well in Fig. 2.

Taking  $c = -3.3$  and 3 as two examples, we further explore the homogenous coexisting behaviors regulated by the initial condition  $x_0$  using local basins of attraction. To measure the dynamical effects of each initial condition, we draw the local basins of attraction in the  $x_0 - y_0$  plane and show the results in Fig. 3(a1) and (b1), where different color regions represent the attractors with different dynamic amplitudes on the  $x$ -coordinate. Obviously, all color regions in Fig. 3(a1) exhibit diagonal symmetry, while all color regions in Fig. 3(b1) are symmetric about the diagonal except

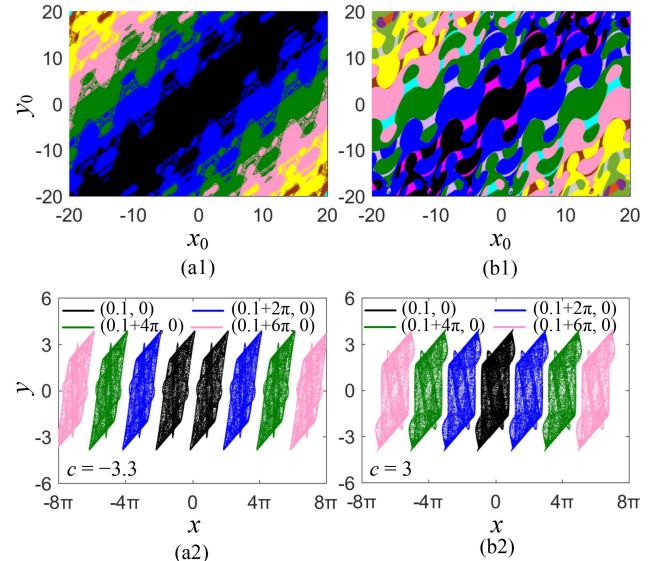


**Fig. 3.** Homogenous coexisting behaviors in Case 1, where (a1) and (b1) represent the local basins of attraction in the  $x_0 - y_0$  plane, and (a2) and (b2) represent the phase diagrams for fixed  $(x_0, y_0) = (0.1 + 2m\pi, 0)$  ( $m = 0, 1, 2, 3$ ). (a) Example 1:  $c = -3.3$ . (b) Example 2:  $c = 3$ .

the black region. It should be noticed that the main color regions in Fig. 3(b1) include black, blue, dark green, pink, and yellow regions, and the area of the black region is only half that of each of the other main color regions. In addition, magenta, light purple, and cyan regions are the attracting regions with different positions of stable points.

Meanwhile, corresponding to the local basins of attraction in Fig. 3(a1) and (b1), the phase diagrams of the homogenous coexisting hyperchaotic attractors for  $(x_0, y_0) = (0.1 + 2m\pi, 0)$  ( $m = 0, 1, 2, 3$ ) are obtained and the results are depicted in Fig. 3(a2) and (b2). As can be seen, the positive and negative parts of the seek attractor pair in Fig. 3(a2) are shifted by the offset  $2m\pi$  along the positive and negative  $x$ -coordinates, respectively, while the seek attractor in Fig. 3(b2) splits into pairs of positive and negative attractors that are shifted by the offset  $2m\pi$  along the positive and negative  $x$ -coordinates, respectively.

Therefore, the homogenous coexisting behaviors can be regulated by the initial condition  $x_0$  in the dynamic amplitudes, indicating the correctness of the theoretical analysis given in Section III-A. However, in the previously published literature, the attractors boosted by initial condition offsets are copied one by one in one direction [33]. Therefore, the homogenous coexisting hyperchaotic attractors in 2D-DNM are radically different from the initial-boosted coexisting behaviors.

#### D. Homogenous Coexisting Behaviors for Case 2

For Case 2, the control parameters and initial conditions are set to  $a = -0.6$ ,  $b = -1$ , and  $(x_0, y_0) = (0.1, 2l\pi)$  ( $l = 0, 1, 2, 3$ ). As increasing the control parameter  $c$  from  $-3.4$  to  $4.6$ , the homogenous coexisting behaviors regulated by the initial conditions are simulated numerically. Thus, the bifurcation diagrams of state variable  $y$  under four sets of initial conditions and the LE spectra under  $(x_0, y_0) = (0.1, 0)$  are described, as

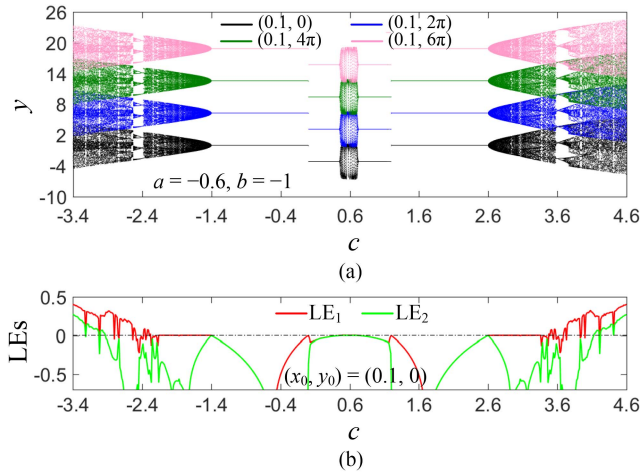


**Fig. 4.** For  $a = -0.6$ ,  $b = -1$ , and  $(x_0, y_0) = (0.1, 2l\pi)$  ( $l = 0, 1, 2, 3$ ) with  $c \in [-3.4, 4.6]$ , homogenous coexisting behaviors regulated by the initial conditions. (a) Bifurcation diagrams of state variable  $y$  under  $(x_0, y_0) = (0.1, 2l\pi)$ . (b) LE spectra under  $(x_0, y_0) = (0.1, 0)$ .

shown in Fig. 4(a) and (b). As can be observed from Fig. 4, the bifurcation diagrams under these four sets of initial conditions have the identical bifurcation structure but different dynamic amplitudes. Moreover, 2D-DNM has the same quasi-periodic route to chaos and shows complex dynamical behaviors of hyperchaos, chaos, quasi-period, period, and stable point. In addition to the bifurcation track bands on the left and right sides, the bifurcation diagrams also exhibit the quasi-periodic track bands around  $c = 0.6$ , leading to another type of homogenous coexisting quasi-periodic behaviors appearing in 2D-DNM.

Taking  $c = -3.3$  and 4.6 as two representative examples, the local basins of attraction are utilized to further investigate the homogenous coexisting behaviors regulated by both initial conditions  $x_0$  and  $y_0$ . The local basins of attraction in the  $x_0 - y_0$  plane are shown in Fig. 5(a1) and (b1), where different color regions represent the attractors with different dynamic amplitudes on the  $x$ - and  $y$ -coordinates. Obviously, the attracting region of each type of attractors is uniformly distributed in blocks on the initial condition plane. There is only one blue block in Fig. 5(a1) and one black block in Fig. 5(b1), while the other blocks appear in pairs in the  $x_0$ -coordinate direction, and the area of each color block is equal.

Correspondingly, when  $(x_0, y_0) = (0.1, 2l\pi)$  ( $l = 0, 1, 2, 3$ ), the phase diagrams of the homogenous coexisting hyperchaotic attractors in Case 2 can be simulated and their numerical results are depicted in Fig. 5(a2) and (b2). As shown in Fig. 5(a2), when  $l = 0$ , 2D-DNM generates a pair of hyperchaotic attractors with left and right parts. When  $l = 1$ , the hyperchaotic attractor is shifted by  $2\pi$  on the positive  $y$ -coordinate as a whole, while on the  $x$ -coordinate, its right part remains unchanged and its left part shifts by  $2\pi$  in the positive direction, resulting in the merging of the two parts. When  $l = 2$ , relative to the case of  $l = 0$ , the two parts of the hyperchaotic attractor are collectively shifted by  $4\pi$  on the positive  $y$ -coordinate and by  $2\pi$  on the positive  $x$ -coordinate. Furthermore, when  $l = 3$ , the two parts of the hyperchaotic attractor as a whole continue to shift by  $2\pi$  on

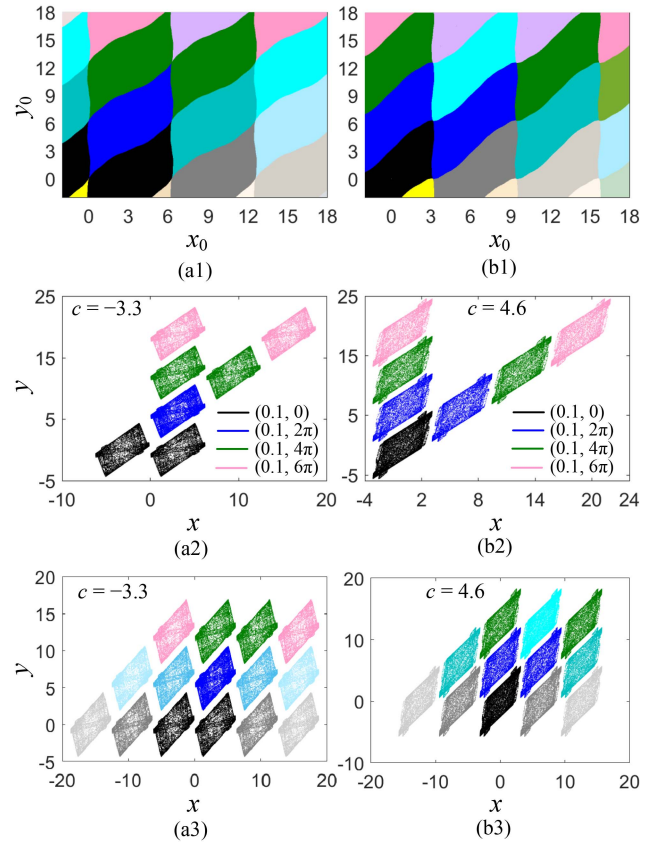


**Fig. 5.** Homogenous coexisting behaviors in Case 2, where (a1) and (b1) represent the local basins of attraction in the  $x_0 - y_0$  plane, (a2) and (b2) represent the phase diagrams for fixed  $(x_0, y_0) = (0.1, 2l\pi)$  ( $l = 0, 1, 2, 3$ ), and (a3) and (b3) represent the phase diagrams for fixed  $(x_0, y_0) = (0.1 + 2m\pi, 2l\pi)$  ( $m, l = 0, 1, 2$ ). (a) Example 1:  $c = -3.3$ . (b) Example 2:  $c = 4.6$ .

the positive  $y$ -coordinate, while the left part remains unchanged and the right part shifts by  $4\pi$  on the positive  $x$ -coordinate. As illustrated in Fig. 5(b2), when  $l = 0$ , 2D-DNM generates a hyperchaotic attractor with single piece. When  $l = 1$ , the hyperchaotic attractor with single piece splits into two pieces, and the whole part is shifted by  $2\pi$  on the positive  $y$ -coordinate, while the right part is shifted by  $2\pi$  on the positive  $x$ -coordinate. When  $l = 2$  and 3, the whole hyperchaotic attractor continues to shift by  $2\pi$  on the positive  $y$ -coordinate, and the right part continues to shift by  $2\pi$  on the positive  $x$ -coordinate.

Furthermore, corresponding to the local basins of attraction shown in Fig. 5(a1) and (b1), the initial conditions are set to  $(x_0, y_0) = (0.1 + 2m\pi, 2l\pi)$  ( $m, l = 0, 1, 2$ ). Thus, the homogenous coexisting hyperchaotic attractors present grid distributions on the  $x - y$  plane, and their phase diagrams are depicted in Fig. 5(a3) and (b3). Therefore, not only the  $y_0$ -offset can regulate the attractor positions on the  $y$ -coordinate, but also the  $x_0$ -offset can regulate the attractor positions on the  $x$ -coordinate. In other words, the attractor plane positions can be controlled by adjusting the  $x_0$ -offset and  $y_0$ -offset.

The above results show that the homogenous coexisting behaviors can be simultaneously regulated by the initial conditions  $x_0$  and  $y_0$  in the dynamic amplitudes, indicating the correctness

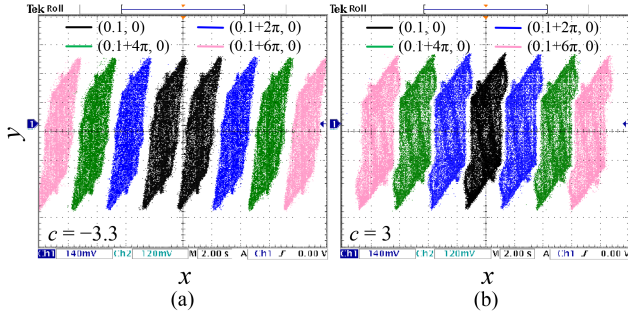


**Fig. 6.** Experimentally measured phase diagrams of the homogenous coexisting attractors in *Case 1*, where  $a = 0.6$ ,  $b = 0.4$ ,  $(x_0, y_0) = (0.1 + 2m\pi, 0)$  ( $m = 0, 1, 2, 3$ ). (a) Example 1:  $c = -3.3$ . (b) Example 2:  $c = 3$ .

of the theoretical analysis given in Section III-B. However, special attention should be paid to the fact that the iterative sequences in the homogenous coexisting behaviors cannot be regulated to different positions by the initial conditions. Therefore, such homogenous coexisting behaviors are essentially different from the initial-boosted coexisting behaviors reported in the literature [21], which, to the knowledge of the authors, have not been investigated.

#### IV. FPGA-BASED DIGITAL IMPLEMENTATION

Continuous chaotic systems are usually implemented with analog circuits, while discrete chaotic systems are more suitable for implementation with digital circuits [34]. In this section, we study the digital implementation of 2D-DNM based on field-programmable gate array (FPGA) technology.

FPGA platform consists of logic units, data processing units, I/O units, and storage units, and is programmed with Verilog hardware description language (HDL). The Verilog HDL can provide a large number of intellectual property (IP) cores confirming to the IEEE 754 standard, such as adder, subtracter, multiplier, to customize the program of the proposed 2D-DNM in Vivado compilation environment. Thus, Xilinx XC7Z020 FPGA development board is employed to digitally implement the 2D-DNM. The Verilog program with preset control parameters and initial conditions can be directly run after compiling and downloading to the FPGA development board. Two AN9767 DAC modules are utilized to convert data signals to analog sequences displayed on the oscilloscope.

Corresponding to the numerical results in Fig. 3(a2) and (b2), the control parameters and initial conditions are first preset to  $a = 0.6$ ,  $b = 0.4$ ,  $c = -3.3$  (or 3), and  $(x_0, y_0) = (0.1+2m\pi, 0)$  ( $m = 0, 1, 2, 3$ ). 2D-DNM is in *Case 1* and can provide the homogenous coexisting hyperchaotic attractors along the  $x$ -coordinate. When the FPGA development board is switched ON, the phase diagrams in the  $x - y$  plane can be measured from FPGA digital platform by the oscilloscope and the measured results are shown in Fig. 6. Therefore, the experimental and numerical results are in perfect agreement.

In the same way, following the numerical results in Fig. 5, the control parameters are then preset to  $a = -0.6$ ,  $b = -1$ , and  $c = -3.3$  (or 4.6). 2D-DNM is in *Case 2*. When the initial conditions

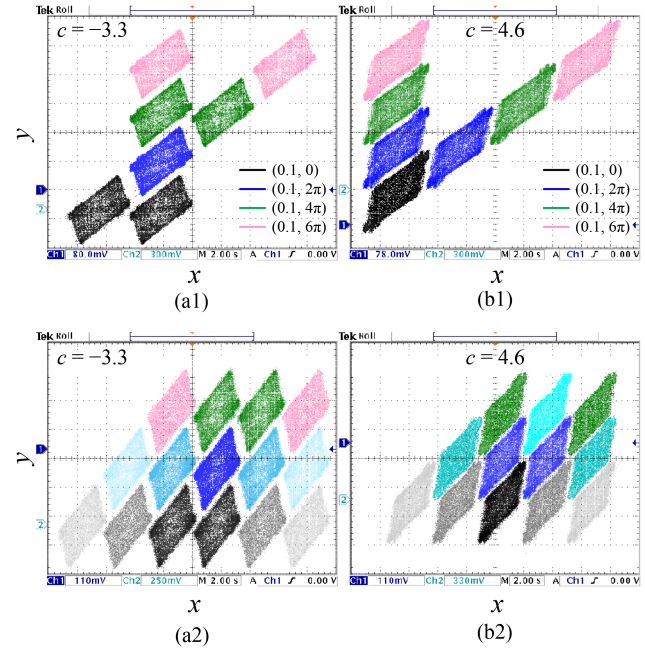


**Fig. 7.** Experimentally measured phase diagrams of the homogenous coexisting attractors in *Case 2*, where  $(x_0, y_0) = (0.1, 2l\pi)$  ( $l = 0, 1, 2, 3$ ) in (a1) and (b1), and  $(x_0, y_0) = (0.1+2m\pi, 2l\pi)$  ( $m, l = 0, 1, 2$ ) in (a2) and (b2). (a) Example 1:  $c = -3.3$ . (b) Example 2:  $c = 4.6$ .

are preconfigured as  $(x_0, y_0) = (0.1, 2l\pi)$  ( $l = 0, 1, 2, 3$ ), the FPGA-based digital platform can generate the phase diagrams of the homogenous coexisting hyperchaotic attractors along the  $y$ -coordinate and the measurement results are shown in Fig. 7(a1) and (b1). While when  $(x_0, y_0) = (0.1+2m\pi, 2l\pi)$  ( $m, l = 0, 1, 2$ ), the homogenous coexisting hyperchaotic attractors present grid distributions on the  $x - y$  plane, and their phase diagrams produced by the FPGA-based digital platform are displayed by the oscilloscope, as depicted in Fig. 7(a2) and (b2). Clearly, the experimental results successfully verify the numerical results.

The experimental results in Figs. 6 and 7 also demonstrate the feasibility and correctness of the FPGA digital platform. Besides, it should be mentioned that the experimental phase diagrams of the homogenous coexisting hyperchaotic attractors starting from different initial conditions are acquired separately on the oscilloscope, and then they are merged into a single picture by Adobe Photoshop.

#### V. PRNG DESIGN AND TESTU01 EXPERIMENT

This section designs eight PRNGs using 2D-DNM under eight groups of control parameters and initial conditions and analyzes their randomness using TestU01 test suite.

##### A. Performance Analyses for Hyperchaotic Sequences

As mentioned above, 2D-DNM can generate hyperchaotic attractors under specific control parameters, and can provide homogenous coexisting hyperchaotic attractors through the control

**TABLE I**  
PERFORMANCE OF FOUR TYPES OF SEEDED HYPERCHAOTIC SEQUENCES

$(a, b, c)$	LE <sub>1</sub> , LE <sub>2</sub>	SpecEn	SampEn	PermEn	CorDim
(0.6, 0.4, -3.3)	0.3218, 0.1348	0.9604	2.1965	6.5351	1.9964
(0.6, 0.4, 3)	0.3686, 0.0964	0.9607	2.1933	6.5271	1.9703
(-0.6, -1, -3.3)	0.3589, 0.2076	0.9599	2.1545	6.5292	1.9862
(-0.6, -1, 4.6)	0.4021, 0.2675	0.9605	2.1342	6.5187	1.9748

**TABLE II**  
PERFORMANCE OF INITIAL-OFFSET CONTROLLED HYPERCHAOTIC SEQUENCES

$(x_0, y_0)$	LE <sub>1</sub> , LE <sub>2</sub>	SpecEn	SampEn	PermEn	CorDim
(0.1, 0)	0.3218, 0.1348	0.9604	2.1965	6.5351	1.9964
(0.1+2 $\pi$ , 0)	0.3202, 0.1341	0.9602	2.1405	6.5354	1.9526
(0.1+4 $\pi$ , 0)	0.3214, 0.1381	0.9604	2.1679	6.5472	1.9456
(0.1+6 $\pi$ , 0)	0.3200, 0.1335	0.9600	2.1955	6.5045	1.9570

of initial-offsets. The iterative sequences of these hyperchaotic attractors have different dynamic amplitudes. To fairly test their performance, we unify these hyperchaotic sequences by performing modulo 1 to them.

We evaluate the performance of the hyperchaotic sequences using two LEs (LE<sub>1</sub>, LE<sub>2</sub>), spectral entropy (SpecEn), sample entropy (SampEn), permutation entropy (PermEn), and correlation dimension (CorDim) [16]. SpecEn is used for the sequence analysis to quantify the amount of information contained in different frequency bands. SampEn is used to measure the sequence regularity. PermEn is a method of the sequence unpredictability based on the frequency of different patterns. And CorDim is a measure of the fractal dimension to characterize the self-similarity and irregularity. During the experiments, the embedding dimensions for SampEn and PermEn are fixed as 1 and 6, respectively, while the embedding dimension and phase space reconstruction delay of CorDim are set to 2 and 1, respectively. Meanwhile, select the hyperchaotic sequences of the state variable  $x$ , and set the lengths of all these hyperchaotic sequences to  $10^5$  for testing.

First, we fix the initial conditions as  $(x_0, y_0) = (0.1, 0)$  and set the control parameters as  $(a, b, c) = (0.6, 0.4, -3.3), (0.6, 0.4, 3), (-0.6, -1, -3.3)$ , and  $(-0.6, -1, 4.6)$ , respectively. Then, 2D-DNM can provide four types of seeded hyperchaotic attractors. Correspondingly, the performance of these seeded hyperchaotic attractors is evaluated and their indicators are listed in Table I. As can be seen, all the generated sequences are hyperchaotic and have large indicators, which demonstrate that these seeded hyperchaotic attractors have excellent ergodicity, low regularity, and high dimensionality in the phase space.

Second, we fix the control parameters as  $(a, b, c) = (0.6, 0.4, -3.3)$  and set the initial conditions as  $(x_0, y_0) = (0.1+2m\pi, 0)$  ( $m = 0, 1, 2, 3$ ), respectively. Then, four initial-offset controlled hyperchaotic sequences can be generated by 2D-DNM, and their performance indicators are calculated and listed in Table II. The results show that the hyperchaotic sequences

controlled by the initial-offsets possess almost the same values on different indicators, indicating the high controllability of these hyperchaotic sequences by the initial conditions. Some previous high-dimensional discrete systems can also generate hyperchaotic sequences, but they have no such nondestructive controllability [35].

### B. PRNGs and Randomness Tests

Chaotic sequences are commonly employed to construct PRNGs owing to their ergodicity, initial value sensitivity and unpredictability. Here, we design eight PRNGs using 2D-DNM under eight groups of control parameters and initial conditions and analyzes their randomness using TestU01 test suite.

The chaotic sequences are represented using floating-point numbers when implemented on FPGA digital platform. Considering practical applications and security requirements, we select 1-D chaotic sequences and convert them into binary numbers. Denote  $\{X_n|n = 1, 2, 3, \dots\}$  as an iteration sequence provided by 2D-DNM. By performing modulo 1 to  $X_n$ , a new iteration sequence  $X_m$  within the range  $[0, 1]$  is obtained. Then, a PRNG can be designed as follows:

$$\text{PRNG} = \lfloor X_m \times K \rfloor \bmod L \quad (23)$$

where  $K = 10^9$  is a magnification factor and  $L = 2^i$  is a positive number, the function  $\lfloor \bullet \rfloor$  denotes the upward rounding operation. It is obvious that each pseudorandom number (PRN) can produce eight binary numbers when  $i = 8$ .

To provide a convincing and fair testing result, we utilize the open-source test suite TestU01 [36] to test the randomness of our PRNGs. TestU01 is much more stringent and can evaluate much longer random sequences than other test standards such as NIST. Our test uses eight batteries, including *FIPS-140-2*, *PseudoDIEHARD*, *Alphabit*, *Rabbit*, *BlockAlphabit*, *Small-Crush*, *Crush*, *BigCrush*, to test the randomness of our PRNG. Each battery applies several statistical tests to the tested sequences and each one generates a  $p$ -value. If all the generated  $p$ -values fall into the interval  $[0.0010, 0.9990]$ , the sequences pass the corresponding statistical test. Significantly, the *Crush* with 144 statistical tests and the *BigCrush* with 160 statistical tests are two extremely stringent batteries and a PRNG shows high randomness if it can pass them.

Since the *Rabbit*, *Alphabit*, and *BlockAlphabit* batteries can take a sequence with any take length as input, we set the length of the inputted sequence as 32 GB in our experiments. The lengths of the inputted sequences for the other five batteries are determined by the test suite. To test the performance of 2D-DNM, we evaluate eight groups of PRNGs generated by 2D-DNM with different control parameters and initial conditions. Specifically, we first change the control parameter  $c$  on the PRNGs for both cases of 2D-DNM, shown in Table III. The initial conditions are set as  $(x_0, y_0) = (0.1, 0)$  and blurred by ambient noise. As can be observed, the PRNGs for *Case 1* and *Case 2* can pass all batteries of TestU01. In addition, we fix the control parameters as  $(a, b, c) = (0.6, 0.4, -3.3)$  and choose different  $m$  in the initial condition. The results of this situation shown in Table IV also

TABLE III

TESTU01 RESULTS FOR DIFFERENT LENGTHS OF PRNs PROVIDED BY 2D-DNM UNDER FOUR CONTROL PARAMETERS

TestU01 Standard Test Suites*		PRNGs for Case 1		PRNGs for Case 2	
Sub-tests	Data size	$c = -3.3$	$c = 3$	$c = -3.3$	$c = 4.6$
FIPS-140-2	19 kB	16/16	16/16	16/16	16/16
PseudoDIEHARD	5 GB	126/126	126/126	126/126	126/126
Alphabit	32 GB	17/17	17/17	17/17	17/17
Rabbit	32 GB	40/40	40/40	40/40	40/40
BlockAlphabit	32 GB	102/102	102/102	102/102	102/102
SmallCrush	6 GB	15/15	15/15	15/15	15/15
Crush	1 TB	144/144	144/144	144/144	144/144
BigCrush	10 TB	160/160	160/160	160/160	160/160

Note: \* The detailed test results can refer to [https://github.com/charlesbao/TestU01\\_Randomness\\_Tests](https://github.com/charlesbao/TestU01_Randomness_Tests).

TABLE IV

TESTU01 RESULTS FOR DIFFERENT LENGTHS OF PRNs PROVIDED BY 2D-DNM UNDER FOUR INITIAL CONDITIONS

TestU01 Standard Test Suites*		PRNGs under $(x_0, y_0) = (0.1+2m\pi, 0)$			
Sub-tests	Data size	$m = 0$	$m = 1$	$m = 2$	$m = 3$
FIPS-140-2	19 kB	16/16	16/16	16/16	16/16
PseudoDIEHARD	5 GB	126/126	126/126	126/126	126/126
Alphabit	32 GB	17/17	17/17	17/17	17/17
Rabbit	32 GB	40/40	40/40	40/40	40/40
BlockAlphabit	32 GB	102/102	102/102	102/102	102/102
SmallCrush	6 GB	15/15	15/15	15/15	15/15
Crush	1 TB	144/144	144/144	144/144	144/144
BigCrush	10 TB	160/160	160/160	160/160	160/160

pass all the batteries. Hence, 2D-DNM shows high performance in the application of PRNGs.

The advantages of 2D-DNM for the designed PRNGs are as follows. 1) The hyperchaotic sequences generated by 2D-DNM exhibit excellent chaos complexity, as evidenced in Tables I and II. This feature results in the generated PRNs with a significantly high degree of unpredictability. 2) 2D-DNM can simultaneously generate two hyperchaotic sequences, each of which can be utilized for generating PRNs.

The disadvantages are summarized as follows. 1) The designed PRNG uses only a single hyperchaotic sequence, whereas 2D-DNM can generate two hyperchaotic sequences. This may result in additional computing costs. 2) Each outputted state contains many bits, possibly exceeding 32 bits. However, when generating PRNs, only 8 bits are utilized and the remaining bits are discarded. This may lead to a loss of efficiency.

### C. Designed PRNG Hardware Device

For convenience of application, a logic circuit is designed based on the corresponding algorithm for the PRNG. The circuit is implemented on a Xilinx XC7Z020 FPGA board and is driven by the supplied 50 MHz PL system clock source. Double precision floating point numbers combined with fixed point numbers of sufficient bit-width participate in the computation

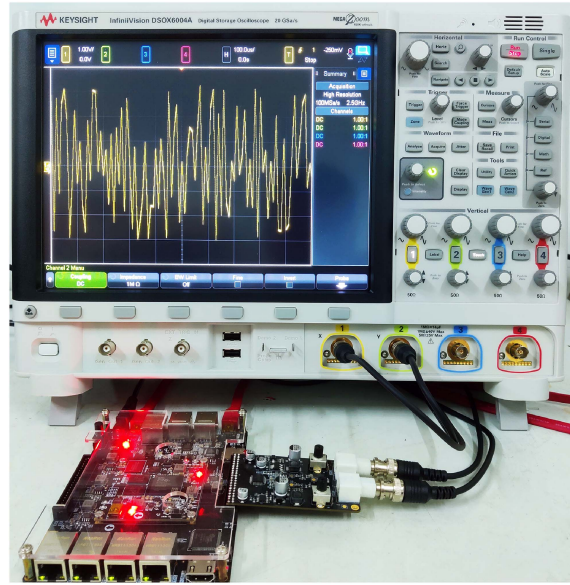


Fig. 8. PRNG hardware device based on the FPGA-based platform.

to ensure adequate data precision. To facilitate the oscilloscope observations, the results of fixed-point data are fixed to intercept 14 bits and converted to analog signals for observation via AN9767 DAC. Here, the initial conditions are determined as  $(x_0, y_0) = (0.1, 0)$ , and the control parameters are selected as  $(a, b, c) = (0.6, 0.4, -3.3)$ . Fig. 8 shows the PRNG hardware device based on the FPGA-based platform. As can be seen from the figure, the proposed PRNG can be efficiently implemented on an FPGA device and its randomness is also well preserved.

Discrete chaotic maps can also be realized by analog circuits and can engender true chaos [37]. However, it is difficult to apply to PRNG due to the uncontrollable initial conditions. The digitally circuit-implemented PRNG hardware device can generate the same pseudorandom number sequences by setting PRN seeds, which makes it widely used in different industrial information fields, and can be further improved its throughput by increasing the input clock frequency. In addition, the FPGA-based PRNG hardware device has higher performance and reliability than that based on analog circuits which are affected by parasitic parameters.

## VI. CONCLUSION

Introducing periodic nonlinearities into some existing offset-boostable systems can achieve the initial-offset-control coexisting dynamics. In this article, we proposed 2D-DNM using sine activation function. The model can be divided into two categories: *Case 1* with finite invariant points and *Case 2* with infinite invariant points, both of which have parameter-dependent stability types. The mechanisms of initial-offset-control coexisting dynamics were investigated theoretically and the homogenous coexisting behaviors were revealed numerically. The results showed that, the homogenous coexisting attractors are controlled in one direction by one initial-offset for *Case 1* and

in two directions by two initial-offsets for *Case 2*. The homogeneous coexisting hyperchaotic attractors were acquired experimentally on FPGA digital platform. Besides, eight PRNGs were developed using 2D-DNM under different model parameter and initial condition settings, and the test results by TestU01 suite demonstrated that these PRNGs own high randomness without chaos degradation. In conclusion, 2D-DNM has high flexibility in generating initial-offset-control coexisting hyperchaos with excellent performance, which is suitable for many industrial applications [11], [16], [21] and worthy of further study.

## REFERENCES

- [1] H. Lin, C. Wang, L. Cui, Y. Sun, C. Xu, and F. Yu, "Brain-like initial-boosted hyperchaos and application in biomedical image encryption," *IEEE Trans. Ind. Informat.*, vol. 18, no. 12, pp. 8839–8850, Dec. 2022.
- [2] S. Kumar, J. P. Strachan, and R. S. Williams, "Chaotic dynamics in nanoscale NbO<sub>2</sub> Mott memristor for analogue computing," *Nature*, vol. 548, no. 7667, pp. 318–321, Aug. 2017.
- [3] V. K. Sangwan et al., "Multi-terminal memtransistors from polycrystalline monolayer molybdenum disulfide," *Nature*, vol. 554, no. 25747, pp. 500–504, Feb. 2018.
- [4] A. Serb, J. Bill, A. Khat, R. Berdan, R. Legenstein, and T. Prodromakis, "Unsupervised learning in probabilistic neural networks with multi-state metal-oxide memristive synapses," *Nature Commun.*, vol. 7, Sep. 2016, Art. no. 12611.
- [5] P. Yao et al., "Fully hardware-implemented memristor convolutional neural network," *Nature*, vol. 577, no. 7550, pp. 641–646, Jan. 2020.
- [6] Q. Hong, H. Chen, J. Sun, and C. Wang, "Memristive circuit implementation of a self-repairing network based on biological astrocytes in robot application," *IEEE Trans. Neural Netw. Learn. Syst.*, vol. 33, no. 11, pp. 2106–2120, Nov. 2022.
- [7] Z. T. Njitacke et al., "Hamiltonian energy and coexistence of hidden firing patterns from bidirectional coupling between two different neurons," *Cogn. Neurodyn.*, vol. 16, pp. 899–916, Aug. 2022.
- [8] H. Bao, M. Hua, J. Ma, M. Chen, and B. Bao, "Offset-control plane coexisting behaviors in two-memristor-based Hopfield neural network," *IEEE Trans. Ind. Electron.*, vol. 70, no. 10, pp. 10526–10535, Oct. 2023.
- [9] S. Ding, N. Wang, H. Bao, B. Chen, H. Wu, and Q. Xu, "Memristor synapse-coupled piecewise-linear simplified Hopfield neural network: Dynamics analysis and circuit implementation," *Chaos, Solitons, Fractals*, vol. 166, Jan. 2023, Art. no. 112899.
- [10] K. Li, H. Bao, H. Li, J. Ma, Z. Hua, and B. Bao, "Memristive Rulkov neuron model with magnetic induction effects," *IEEE Trans. Ind. Informat.*, vol. 18, no. 3, pp. 1726–1736, Mar. 2022.
- [11] X. Meng, P. Rozycki, J.-F. Qiao, and B. M. Wilamowski, "Nonlinear system modeling using RBF networks for industrial application," *IEEE Trans. Ind. Informat.*, vol. 14, no. 3, pp. 931–940, Mar. 2018.
- [12] E. Zeraoulia, *Robust Chaos and Its Applications*, vol. 79. Singapore: World Science, 2012.
- [13] M. Han, R. Zhang, T. Qiu, M. Xu, and W. Ren, "Multivariate chaotic time series prediction based on improved grey relational analysis," *IEEE Trans. Syst., Man, Cybern., Syst.*, vol. 49, no. 10, pp. 2144–2154, Oct. 2019.
- [14] J. Zheng, H. Hu, and X. Xia, "Applications of symbolic dynamics in counteracting the dynamical degradation of digital chaos," *Nonlinear Dyn.*, vol. 94, no. 2, pp. 1535–1546, Oct. 2018.
- [15] S. Chen, S. Yu, J. Lü, G. Chen, and J. He, "Design and FPGA-based realization of a chaotic secure video communication system," *IEEE Trans. Circuits Syst. Video Technol.*, vol. 28, no. 9, pp. 2359–2371, Sep. 2018.
- [16] H. Li, Z. Hua, H. Bao, L. Zhu, M. Chen, and B. Bao, "Two-dimensional memristive hyperchaotic maps and application in secure communication," *IEEE Trans. Ind. Electron.*, vol. 68, no. 10, pp. 9931–9940, Oct. 2021.
- [17] Z. Hua, Y. Zhou, and B. Bao, "Two-dimensional sine chaotification system with hardware implementation," *IEEE Trans. Ind. Informat.*, vol. 16, no. 2, pp. 887–897, Feb. 2020.
- [18] Y. Deng and Y. Li, "Bifurcation and bursting oscillations in 2D non-autonomous discrete memristor-based hyperchaotic map," *Chaos, Solitons, Fractals*, vol. 150, Sep. 2021, Art. no. 111064.
- [19] H. Bao, H. Li, Z. Hua, Q. Xu, and B. Bao, "Sine-transform-based memristive hyperchaotic model with hardware implementation," *IEEE Trans. Ind. Informat.*, vol. 19, no. 3, pp. 2792–2801, Mar. 2023.
- [20] Z. Hua, Y. Chen, H. Bao, and Y. Zhou, "Two-dimensional parametric polynomial chaotic system," *IEEE Trans. Syst., Man, Cybern., Syst.*, vol. 52, no. 7, pp. 4402–4414, Jul. 2022.
- [21] H. Bao, Z. Hua, H. Li, M. Chen, and B. Bao, "Memristor-based hyperchaotic maps and application in auxiliary classifier generative adversarial nets," *IEEE Trans. Ind. Informat.*, vol. 18, no. 8, pp. 5297–5306, Aug. 2022.
- [22] H. Gu, C. Li, Y. Li, X. Ge, and T. Lei, "Various patterns of coexisting attractors in a hyperchaotic map," *Nonlinear Dyn.*, vol. 111, no. 8, pp. 7808–7818, Apr. 2023.
- [23] C. Li and J. C. Sprott, "An infinite 3-D quasiperiodic lattice of chaotic attractors," *Phys. Lett. A*, vol. 382, no. 8, pp. 581–587, Feb. 2018.
- [24] Z. T. Njitacke, J. D. D. Nkakop, V. F. Signing, N. Tsafack, M. E. Sone, and J. Awrejcewicz, "Novel extreme multistable tabu learning neuron: Circuit implementation and application to cryptography," *IEEE Trans. Ind. Informat.*, vol. 19, no. 8, pp. 8943–8952, Aug. 2023.
- [25] S. Zhang, C. Li, J. Zheng, X. Wang, Z. Zeng, and G. Chen, "Memristive autapse-coupled neuron model with external electromagnetic radiation effects," *IEEE Trans. Ind. Electron.*, vol. 70, no. 11, pp. 11618–11627, Nov. 2023.
- [26] H. Lin, C. Wang, C. Xu, X. Zhang, and H.H.C. Iu, "A memristive synapse control method to generate diversified multi-structure chaotic attractors," *IEEE Trans. Comput.-Aided Des. Integr. Circuits Syst.*, vol. 42, no. 3, pp. 942–955, Mar. 2023.
- [27] Y. Li, C. Li, S. Zhang, G. Chen, and Z. Zeng, "A self-reproduction hyperchaotic map with compound lattice dynamics," *IEEE Trans. Ind. Electron.*, vol. 69, no. 10, pp. 10564–10572, Oct. 2022.
- [28] C. Li, G. Chen, X. Liao, and J. Yu, "Hopf bifurcation and chaos in tabu learning neuron models," *Int. J. Bifurcation Chaos*, vol. 15, no. 8, pp. 2633–2642, Aug. 2005.
- [29] J. C. Sprott, "A proposed standard for the publication of new chaotic systems," *Int. J. Bifurcation Chaos*, vol. 21, no. 9, pp. 2391–2394, Sep. 2011.
- [30] M. Xiao and J. Cao, "Bifurcation analysis on a discrete-time tabu learning model," *J. Comput. Appl. Math.*, vol. 220, no. 1-2, pp. 725–738, Oct. 2008.
- [31] H. Bao, C. Chen, Y. Hu, M. Chen, and B. Bao, "2-D piecewise-linear neuron model," *IEEE Trans. Circuits Syst. II*, vol. 68, no. 4, pp. 1453–1457, Apr. 2021.
- [32] B. Bao, L. Hou, Y. Zhu, H. Wu, and M. Chen, "Bifurcation analysis and circuit implementation for a tabu learning neuron model," *Int. J. Electron. Commun. (AEÜ)*, vol. 121, no. 3, May 2020, Art. no. 153235.
- [33] Q. Lai, C. Lai, H. Zhang, and C. Li, "Hidden coexisting hyperchaos of new memristive neuron model and its application in image encryption," *Chaos, Solitons, Fractals*, vol. 158, May 2022, Art. no. 112017.
- [34] D. Murillo-Escobar, M. Á. Murillo-Escobar, C. Cruz-Hernández, A. Arellano-Delgado, and R. M. López-Gutiérrez, "Pseudorandom number generator based on novel 2D Hénon-Sine hyperchaotic map with microcontroller implementation," *Nonlinear Dyn.*, vol. 111, no. 7, pp. 6773–6789, Apr. 2023.
- [35] Z. Hua, Y. Zhang, H. Bao, H. Huang, and Y. Zhou, "*n*-dimensional polynomial chaotic system with applications," *IEEE Trans. Circuits Syst. I*, vol. 69, no. 2, pp. 784–797, Feb. 2022.
- [36] A. L. B. III et al., "SP 800-22 rev. 1a. A statistical test suite for random and pseudorandom number generators for cryptographic applications." Nat. Inst. Std. Technol., Gaithersburg, MD, USA, Tech. Rep. SP 800-22, 2010.
- [37] P. S. Paul, M. Sadia, M. R. Hossain, B. Muldrey, and M. S. Hasan, "Cascading CMOS-based chaotic maps for improved performance and its application in efficient RNG design," *IEEE Access*, vol. 10, pp. 33758–33770, Apr. 2022.



**Han Bao** (Member, IEEE) received the B.S. degree in landscape design from the Jiangxi University of Finance and Economics, Nanchang, China, in 2015, the M.S. degree in art and design from Changzhou University, Changzhou, China, in 2018, and the Ph.D. degree in nonlinear system analysis and measurement technology from the Nanjing University of Aeronautics and Astronautics, Nanjing, China, in 2021.

In 2019, he visited the Computer Science Department, The University of Auckland, New Zealand. He is currently a Lecturer with the School of Microelectronics and Control Engineering, Changzhou University. His research interests include memristive neuromorphic circuit, nonlinear circuits and systems, and artificial intelligence.



**Zhuowu Wang** received the B.S. degree in automation from Changzhou University, Changzhou, China, in 2022. He is currently working toward the M.S. degree in electronics science and technology with the School of Microelectronics and Control Engineering, Changzhou University.

His research interests include discrete neuron models and networks.



**Zhongyun Hua** (Senior Member, IEEE) received the B.S. degree from Chongqing University, Chongqing, China, in 2011, and the M.S. and Ph.D. degrees from the University of Macau, Macau, China, in 2013 and 2016, respectively, all in software engineering.

He is currently an Associate Professor with the School of Computer Science and Technology, Harbin Institute of Technology, Shenzhen, China. His current research interests include chaotic system, multimedia security, and secure

cloud computing.

Dr. Hua has been recognized as a "Highly Cited researcher 2022."



**Xihong Yu** received the B.S. degree in electronic information engineering from the Huaihe College of Changzhou University, Taizhou, China, in 2021. He is currently working toward the M.S. degree in electronic science and technology in the School of Microelectronics and Control Engineering, Changzhou University, Changzhou, China.

His research interests include memristive neural networks, and nonlinear circuits and systems.



**Quan Xu** (Member, IEEE) received the B.S. degree in physics from Huaiyin Normal University, Huaiyin, China, in 2005, and the Ph.D. degree in optical engineering from the University of Electronic Science and Technology of China, Chengdu, China, in 2011.

In 2018, he visited the Electrical Engineering and Electronics Department, The University of Liverpool, U.K. He is currently an Associate Professor with the School of Microelectronics and Control Engineering, Changzhou University, Changzhou, China. His research interests include memristor and memristive neuromorphic circuit.



**Bocheng Bao** (Member, IEEE) received the B.S. and M.S. degrees in electronic engineering from the University of Electronics Science and Technology of China, Chengdu, China, in 1986 and 1989, respectively, and the Ph.D. degree in information and communication engineering from the Nanjing University of Science and Technology, Nanjing, China, in 2010.

From 2008 to 2011, he was a Professor with the School of Electrical and Information Engineering, Jiangsu University of Technology, Changzhou, China. He was a Professor with the School of Microelectronics and Control Engineering, Changzhou University, Changzhou. In 2013, he visited the Department of Electrical and Computer Engineering, University of Calgary, Calgary, AB, Canada. His research interests include neuromorphic circuits, power electronic circuits, and nonlinear circuits and systems.

Dr. Bao was a recipient of the IET Premium Award in 2018 and selected as the Highly Cited Researcher 2020, 2021, and 2022 in Cross-Field.